Journal of Materials Research and Technology 27 (2023) 4891–4907

Contents lists available at ScienceDirect

Journal of Materials Research and Technology

journal homepage: www.elsevier.com/locate/jmrt

Tailoring the *in-situ* formation of intermetallic phases in the self-lubricating Al–WS_2 composite for enhanced tribological performance with wear track evolution analysis

Peifeng Li [a], Nesma T. Aboulkhair [b,c], Julan Wu [a], Kah L. Leng [a], Deyu Yang [a], Adam T. Clare [d,e], Xianghui Hou [a], Fang Xu [a,*]

[a] *Faculty of Engineering, University of Nottingham, University Park, Nottingham, NG7 2RD, UK*
[b] *Centre for Additive Manufacturing, Advanced Manufacturing Building, University of Nottingham, NG8 1BB, UK*
[c] *Additive Manufacturing Laboratory, Advanced Materials Research Centre (AMRC), Technology Innovation Institute (TII), Masdar City, P.O. 9639, Abu Dhabi, United Arab Emirates*
[d] *Advanced Component Engineering Laboratory (ACEL), University of Nottingham, Nottingham, NG7 2RD, UK*
[e] *Department of Mechanical, Materials and Manufacturing Engineering, Faculty of Science and Engineering, University of Nottingham China, 199 Taikang East Road, University Park, Ningbo, 315100, China*

ARTICLE INFO

Keywords:
Sliding wear
Metal-matrix composite
Lubricant additives
Hardness
Electron microscopy

ABSTRACT

Self-lubricating aluminium matrix composites with enhanced tribological properties are sought for weight critical applications. In previous studies, the Al composites incorporating the solid lubricant WS_2 have been shown to reduce both the coefficient of friction and wear rate, positioning them as promising candidates in various tribological applications (e.g. automotive industry). However, the impact of interfacial reactions between Al and WS_2 during composite production on tribological performance has still not yet been explored. This study highlights the hardening effect of the reaction products. Despite some literature assuming a negative impact of these reactions as they consume WS_2 in the composites, this study presents evidence that this cannot be generalised for the overall outcome. Interestingly, a controlled amount is shown to be beneficial for tribological properties. In this work, the tribological influence of the Al–W intermetallic structure forming during spark plasma sintering of the Al–WS_2 composites was investigated. The microstructure was tailored by adjusting the manufacturing temperature between 500 and 600 °C. The Al–WS_2 fabricated at 580 °C exhibited the lowest coefficient of friction and specific wear rate (reduced by 20 % and 97 %, respectively, compared to the one fabricated at 500 °C. Furthermore, the worn surface morphology in different stages during friction was evaluated by a novel wear track evolution analysis. This study confirmed that offering a balance between the fraction of solid lubricants and *in-situ* formed hard intermetallic structure is crucial to the effective formation a protective layer on the worn surface.

1. Introduction

Aluminium alloys and aluminium matrix composites have garnered increasing attention in engineering sectors, such as automotive, due to their lightweight, high corrosion resistance, and high specific strength [1]. However, aluminium's poor wear resistance and high coefficient of friction (COF) reduce its energy efficiency and component life, which limit its use in tribological applications. Liquid-based lubricants are typically used between parts in dynamic contact applications, such as zinc dialkyldithiophosphate additives (ZDDP) [2], but these contain phosphorous substances that can pose adverse impacts on the environment. Liquid-based lubricants also require replenishment over time and are ineffective in some environments, such as high temperatures [3]. Hard coatings can be used to improve wear resistance, but challenges in refilling and the lack of interfacial strength with the substrate materials limited their structural performance [4]. Towards this end, self-lubricating Al metal matrix composites (MMCs) incorporating solid lubricants were developed to meet the demand for lightweight engineering materials in the automotive sector where the tribological properties are critical. Solid lubricants, such as graphite and transition

* Corresponding author. Room C46 Coates Building, University Park, Nottingham, NG7 2RD, UK.
E-mail address: fang.xu@nottingham.ac.uk (F. Xu).

https://doi.org/10.1016/j.jmrt.2023.10.157
Received 20 July 2023; Accepted 16 October 2023
Available online 19 October 2023

metal chalcogenides, are comprised of a lamellar crystal structure where the interaction between the atoms is through weak Van der Waals forces between the layers. These lubricants can be sheared parallel to the layers when bearing loads, hence reducing friction. Incorporating solid lubricants into the metal matrix enables a self-regulated continuous supply of lubricants forming a tribo-layer during contact [5].

It is well understood that introducing some carbon-based additives into Al alloys by conventional methods often causes reduction in strength and ductility, which is detrimental to wear performance, regardless of the lowered coefficient of friction [6]. For example, graphite is the most widely studied solid lubricant owing to its availability and low price [7], but it agglomerates easily in the matrix due to the lack of bonding with Al, causing a drop in hardness and therefore wear resistance. In contrast, transition metal chalcogenides, such as MoS_2 [8] and WS_2 [9], exhibit better wear resistance as a result of the affinity of sulphur towards the metallic atoms [10], and their performance is far superior to graphite in dry conditions [11]. Compared to MoS_2, WS_2 is often more expensive but offers better tribological performance at high temperatures (above 390 °C) [12]. There are two types of WS_2, 2H (flat-sheet shaped) and IF (inorganic fullerene-like) WS_2 according to its molecular structure. As previous studies revealed, both types can enhance tribological performance when incorporated into Al MMCs. For instance, Niste et al. [11] found that the addition of 20 wt% WS_2 is effective in reducing the wear rate and coefficient of friction (COF) at both room and elevated temperatures (up to 200 °C) compared to pure Al, as a tribo-layer can form on the surface during friction, enhancing the wear resistance of the part.

Spark plasma sintering (SPS) is an advanced powder metallurgy technique that consolidates powder feedstock with the simultaneous application of pulsed current and uniaxial pressure. The technique allows sintering at lower temperatures in relatively short time compared to other conventional methods [13]. The tribological behaviour of SPS processed Al–WS_2 composites has interested numerous researchers, and their studies have shown improved tribological properties compared to the unreinforced Al. Vaziri et al. [14] reported a decrease in both the COF and wear loss at room temperature with increasing the WS_2 content up to 8 wt% when a plateau was reached. Rengifo et al. [15] showed that the COF and wear rate of Al-2vol% WS_2 were lower than pure Al at room temperature and 200 °C with a more pronounced lubricating effect at the elevated temperature. Despite the abundance of literature focussing on the performance of such composite, there is a lack of studies with regard to the interactions between Al and WS_2 during processing, notwithstanding the fact that the chemical reactions between metals and transition metal chalcogenides are thermodynamically favourable [16]. Some studies claimed an adverse effect of these reactions since they reduce the lubricant content in the final composite [17], although this assumption was not supported by experimental evidence. On the contrary, our previous results [18] showed that the *in-situ* formation of the Al–W intermetallic phase during SPS at the Al–WS_2 interfaces can contribute to increasing the hardness, potentially improving the wear resistance.

In this work, we explore the *in-situ* formation mechanisms of this Al–W intermetallic phase in the composite to help maximise the tribological performance of this composite for their potential applications for automotive parts, such as, engine blocks and pistons. To achieve this, microstructural tailoring was realised via varying the SPS processing temperature, which enabled controlling the amount of the resultant intermetallic phase and returned considerable variations in the tribological behaviour of the prepared composites. The intriguing findings in this study confirmed that neither the absence nor excess of interfacial reaction products provided desirable properties, whereas a balanced proportion between the *in-situ* formed Al–W phase and unreacted WS_2 led to the best tribological performance. Moreover, the tribological analysis of the parts fabricated at various temperatures was conducted not only by comparing the COF and wear rate values, but also by establishing their correlation with the wear volume via a new wear track evolution analysis method. This novel analysis approach can facilitate the understanding of the conditions under which the tribo-layer forms to protect the bulk material of the composite. The approach can be translated to studying the tribological behaviour evolutions of other solid materials in the future.

2. Materials and methods

2.1. Materials

In line with numerous previous studies, such as [11,14], pure Al was selected as the matrix material instead of the alloy to isolate the results for investigating the effect of WS_2 on Al exclusively. Gas atomised Al powder (purity 99.7 %), with a generally spherical morphology and a 20–63 μm size range (Fig. 1a), was acquired from Carpenter Additive (USA). The solid lubricant 2H–WS_2 powder (purity 99 %) was supplied by Sigma-Aldrich (USA) with a flake-shaped morphology agglomerated in the form of clusters, ranging from several hundred nanometres to several microns (Fig. 1b and c). To prepare the feedstock mixture for SPS processing of the composite samples, the Al powder was mixed with 10-wt% WS_2 using a Resodyn™ resonance acoustic mixer LabRAM 1 (USA) with the gravitational force and mixing time set to 70G and 3 min, respectively. The WS_2 weight ratio was selected as 10 % since this content was proven effective in lubrication by our internal preliminary studies and the literature [15]. Scanning electron microscopy (SEM), using an FEI 650 Quanta scanning electron microscope (USA), equipped with a tungsten filament source, revealed that the produced Al–WS_2 powder mixture had a homogeneous distribution of the constituents without visible agglomeration (Fig. 1d), where the WS_2 particles were well-distributed, coating the surface of Al particles in a parent-satellite fashion. The mixed powder was sieved by a 63 μm woven wire mesh sieve before processing. The particle size distribution (PSD) determined by a Malvern UK Mastersizer 3000 (Fig. 2) showed that compared to the pure Al powder, the Al–WS_2 powder mixture showed another small proportion of particles with sizes ranging from 0.5 to 5.5 μm, due to some small-scale clustering of WS_2 flakes. This led to a small decrease in the PSD value from $D_{10} = 22.3$ μm, $D_{50} = 37.7$ μm, $D_{90} = 65.1$ μm (Pure Al powder) to $D_{10} = 20.5$ μm, $D_{50} = 36.4$ μm, $D_{90} = 63.2$ μm (Al–WS_2 powder mixture).

2.2. Spark plasma sintering of Al–WS_2 composites

Since ample literature, such as [11,14,18], had already substantiated enhanced tribological performance of Al–WS_2 parts compared to pure Al, the present study focusses on the effect of SPS processing temperatures on the composite's structure and properties, rather than the pure unreinforced material. SPS was performed using an AGUS SPS-630Sx system (Japan). Cylindrical graphite dies (13 mm-diameter) were filled with 1.5 g of Al–WS_2 powder mixture before consolidation. The specimens were processed with pulsed direct current under vacuum (<1 Pa) by pre-programmed parameters (Table S1, supplementary material) which define the maximum target temperature. Internal preliminary trials showed that the composite cannot be consolidated to a dense part under 500 °C, whereas partial melting of Al was observed above 600 °C. Therefore, the range for experiments in this study was set between 500 and 600 °C. The specimens were labelled SPS500, SPS520, SPS540, SPS560, SPS580, SPS600, according to the maximum target temperatures of 500 °C, 520 °C, 540 °C, 560 °C, 580 °C, and 600 °C, reached during the process, respectively. All specimens were fabricated under the maximum target pressure of 50 MPa, guided by previous studies [14,15]. In addition, SPS500HP (higher pressure) was processed under the maximum target temperature 500 °C and pressure 70 MPa to prove that the formation of the intermetallic microstructures, rather than part density, played the critical role in the tribological properties. However, the relevant results and discussions for this particular specimen are provided in the supplementary material (Section S2) for a more coherent

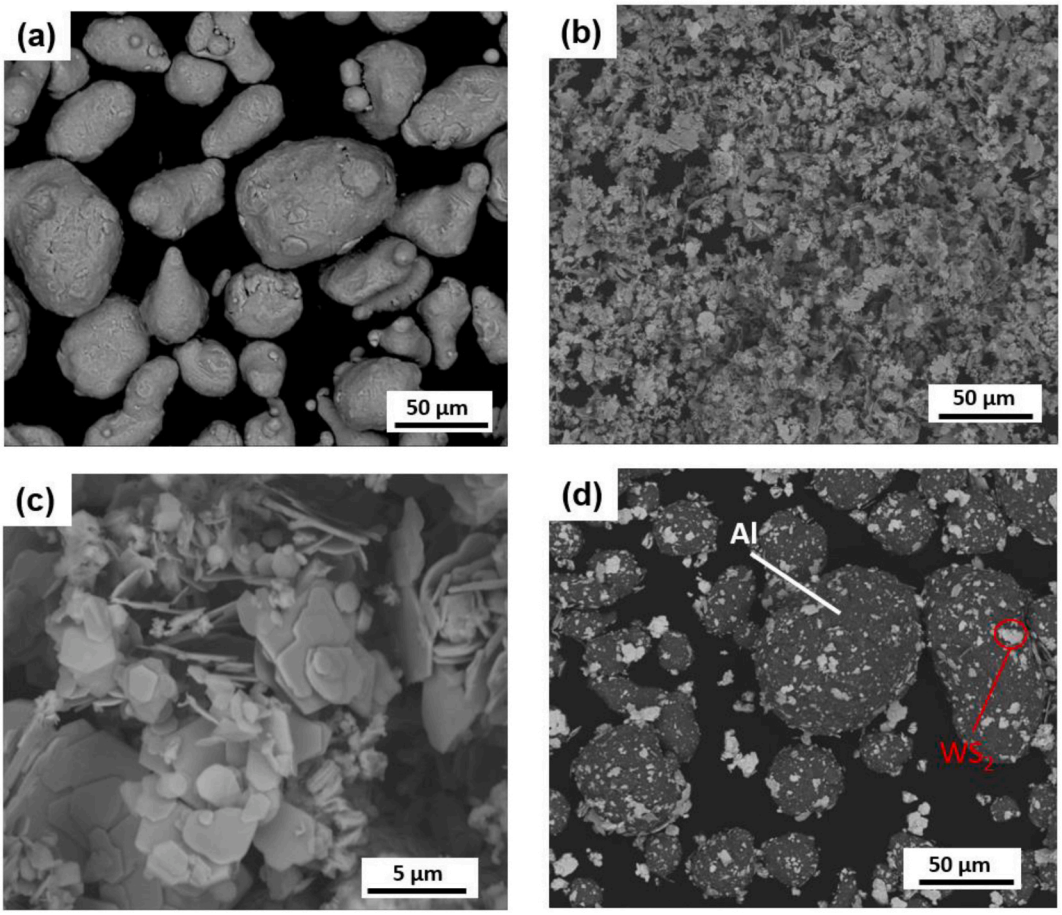

Fig. 1. SEM images showing the morphology of starting powders. (a) pure Al; (b) and (c) WS_2; (d) powder mixing by RAM.

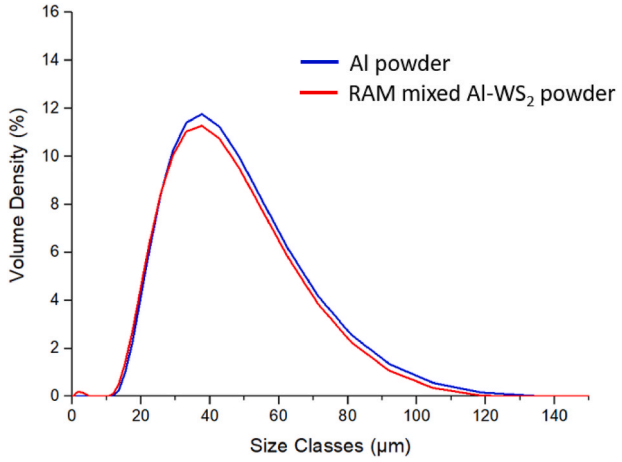

Fig. 2. Particle size distribution of the Al powder and Al–WS_2 powder mixture. (Colour print required).

flow of information in this article. Three repeats were produced at each manufacturing parameters' combination for statistical confidence.

2.3. Metallurgical characterisation and microstructural analysis

The relative density of the fabricated specimens was determined by the Archimedes' method, using water as the immersion medium. The specimens were cross-sectioned and polished along the plane perpendicular to the consolidation/pressing direction, i.e. the x-y plane (Fig. S1, supplementary information), following the standard metallographic protocols [19]. X-ray diffraction (XRD) for phase analysis of the fabricated specimens was performed using a Bruker D8 Advance (USA) with a Cu–Kα X-ray beam source. 2θ scanning was performed between 10 and 90° with the speed of 0.2 s per step and 0.02° per step. The microstructure of starting powders, fabricated parts, wear tracks, subsurfaces after sliding wear, and Si_3N_4 ball counter-body before and after the tribological test was characterised by the FEI 650 Quanta SEM. The images were obtained by a backscatter electron (BSE) detector with an accelerating voltage of 15 kV, and the chemical compositions were detected by Energy-dispersive X-ray (EDX) analysis. TEM lamellas were prepared using the pFIB (Thermofisher scientific formally FEI, USA) via the standard lift-out procedure. Transmission electron microscope (TEM) imaging was conducted with an FEI Tecnai F20 field emission gun scanning transmission electron microscope (FEG-STEM, USA) operated at 200 kV. Conventional TEM micrographs were collected with a Gatan Orius camera.

2.4. Hardness and tribological tests

To assess the strength of Al–WS_2 composites, nano- and micro-hardness was tested as the intended application of this material is green tribology, where the hardness is directly linked to the materials' wear resistance. Therefore, hardness tests are convenient methods to evaluate strength for small cylindrical specimens in this study. For nano- and micro-hardness, and tribological tests, the x-y plane of the samples was ground progressively using 400 to 4000-grit SiC paper, followed by polishing with diamond cloth. The nano-hardness of Al, WS_2, and the intermetallic phases in the composites was tested by a Micro Materials Nanotest™ NTX Platform 3 nanoindenter (UK) according to the ASTM

standard E2546-07 [20] in a depth-controlled mode. A Berkovich diamond tip was used to place 5 indentations on the regions of each microstructural feature in the sample (WS_2 clusters, Al–W intermetallic shell, and Al matrix). The load increased at a constant rate of 0.3 mN/s until a depth of 1000 nm was reached, and then this load was held for 20 s. The indenter tip area function (diamond area function, DAF) and thermal drift correction were accounted for. The nano-hardness was reported based on the mean value of three test runs. A Buehler Wilson VH3100 (USA) Vickers micro-hardness tester equipped with a diamond pyramid indenter was used to measure the micro-hardness of the samples. The load was set to 0.5 kgf for each indentation. A grid pattern of micro-hardness values with an indent-to-indent spacing of 0.5 mm was projected onto the samples' surfaces.

The tribological tests were performed using an Anton Paar TRB^3 tribometer (Austria), according to the ASTM G133-05 standard [21]. The test was conducted at room temperature and atmosphere ambient under dry sliding conditions, while the wear track length, normal load, linear motion frequency, and total cycles were 5 mm, 4 N, 1.5 Hz, and 4000, respectively, as guided by various previous work where similar composite materials were studied [14,15]. The mode of motion was ball-on-flat linear reciprocating sliding wear. A 3.18 mm-radius silicon nitride (Si_3N_4) ball (grade 10, produced by Dejay Ltd., UK) was selected as the counter-body for sliding, for the reason that Si_3N_4 and Al are dissimilar in molecular structure and show great disparity in surface hardness, which leads to negligible chemical interaction between the two during sliding. As a fundamental study, this is advantageous since the complex interference of various counter-body materials in engineering applications can be avoided, thus the wear resistance of the composite materials can be evaluated explicitly. The Si_3N_4 ball appears black in colour. As Fig. 3a shows, the ball has a polished smooth surface. Chemical analysis indicates it comprises Si_3N_4 with the addition of Al_2O_3.

The COF and penetration depth of the ball for each cycle were recorded by the instrument. After three individual runs, the average value of three COF means is reported with standard error, and the average value of specific wear rates is reported with standard deviation.

The *in-situ* wear volume analysis during the tribological test was based on the geometrical relationship between the wear volume, the diameter of the ball, and the penetration depth, as illustrated in Fig. 4. The wear volume (W) is estimated by Equation (1):

$$W = S \bullet L \tag{1}$$

where L is the track length (5 mm), and S is the track cross-section calculated by Equation (2):

$$S = 2\left\{ arcCos[(r-PD)/r] \Big/ 2\pi \bullet \pi r^2 - 1 \Big/ 2 \bullet (r-PD) \bullet \sqrt{r^2-(r-PD)^2} \right\} \tag{2}$$

where r is the radius of the ball (3.18 mm) and PD is the ball penetration depth recorded by the instrument. Combining equations (1) and (2), the relationship between the wear volume and penetration depth (PD) was acquired by Equation (3):

$$W = 2\left\{ arcCos[(3.18mm-PD)/3.18mm] \Big/ 2\pi \bullet \pi(3.18mm)^2 - 1 \Big/ 2 \bullet (3.18mm-PD) \bullet \sqrt{r^2-(r-PD)^2} \right\} \bullet 5mm \tag{3}$$

The theoretical wear volume development during sliding wear is given according to the classic Archard's model [22] of wear prediction, in which the wear volume (V) is calculated by Equation (4):

$$V = (K \bullet W \bullet L)/H \tag{4}$$

where K is the wear coefficient constant of the material, W is the normal load, L is the sliding distance, and H is the hardness of the material.

3. Results and discussion

3.1. Intermetallic phase analysis of Al–WS_2 composites

The relative densities of all fabricated parts are summarised in Fig. 5. SPS is known to consolidate parts with high density [15]. Densification levels of more than 97 % were reached for all specimens, and the mean density showed an increasing trend with rising temperature until 580 °C

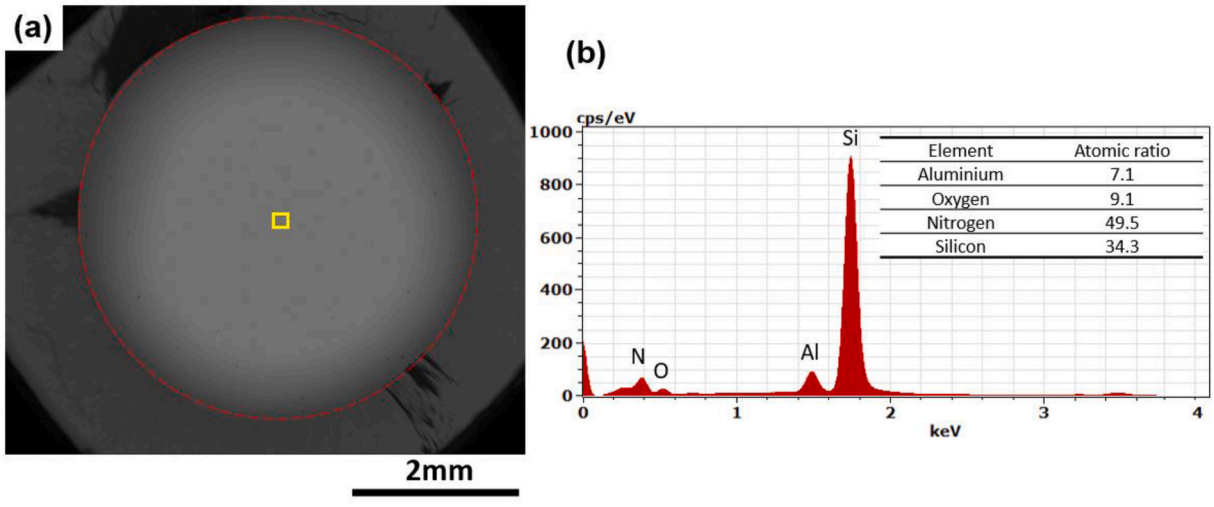

Fig. 3. Characterisation of the counterpart for sliding. (a) SEM image (red circle showing the profile); (b) EDX spectra showing the chemical composition on the selected area in (a) (yellow rectangular box).

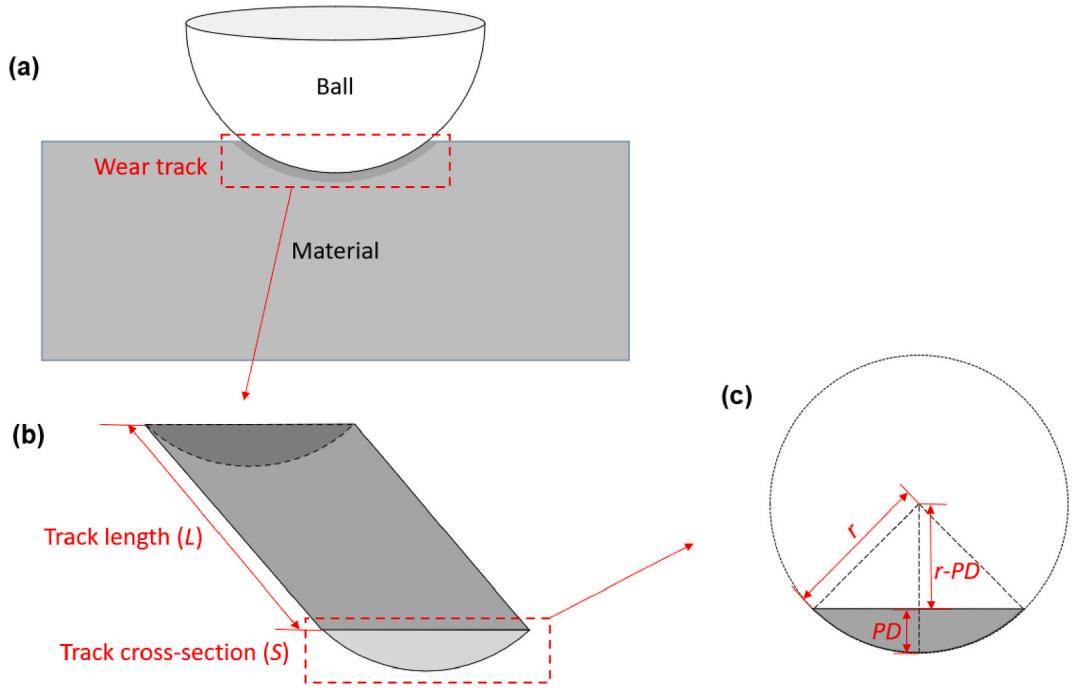

Fig. 4. Schematics showing the methodology of determining the wear volume. (a) wear scar produced by the ball-on-disc wear process; (b) estimated wear volume of the wear track with geometrical features of Track length (*L*) and Track cross-section (*S*); (c) the geometrical relationship among track cross-section area (*S*), the radius of the ball (*r*) and penetration depth (*PD*).

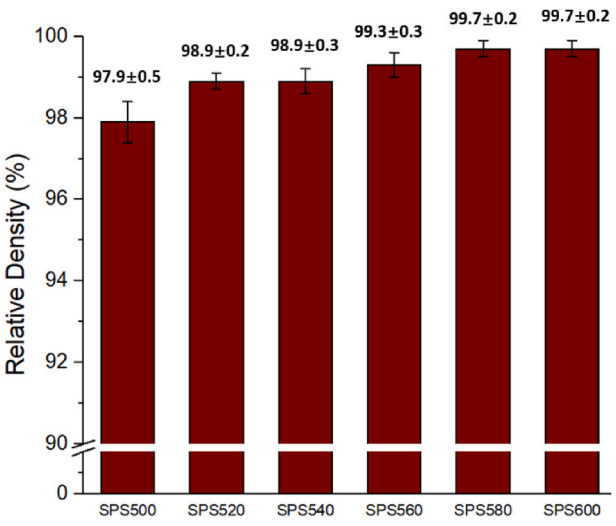

Fig. 5. Relative densities of the Al–WS_2 composites fabricated by SPS under 50 MPa at 500 °C, 520 °C, 540 °C, 560 °C, 580 °C, and 600 °C showing that with increasing processing temperature, the density experienced a rising trend.

when a plateau was reached. This is because elevating the temperature promotes plastic deformation of the material and the escape of air during SPS, which reduces the porosity and thus improves densification.

The phase analysis of the composite fabricated at various temperatures as determined by XRD is presented in the patterns in Fig. 6. For the 500 °C and 520 °C temperatures, the composite only exhibited the strong characteristic peaks corresponding to Al and 2H–WS_2. When the temperature increased to 540 °C and above, the intensity of the main characteristic peak for WS_2, located at $2\theta = 14.3°$ (0 0 2), was significantly weakened. In contrast, some additional peaks of $Al_{12}W$ and Al_5W started to show at 540 °C, and their intensities increased with the temperature. This agrees with our previous study, in which the *in-situ* reactions between Al and WS_2 that formed intermetallic phases during SPS are described in detail and the equation was proposed as Al + WS_2 → Al_xW + Al_2S_3, while the hydrolysation of Al_2S_3 in the atmosphere resulted in its absence in the XRD pattern [18]. At 600 °C, the WS_2 phases still existed but their composition had been drastically reduced as compared to Al, and the intensities of the intermetallic phases reached the highest level within the tested conditions in this study. The weight proportion of the Al:WS_2 in the distinctive samples was calculated using the XRD data via the relative intensity ratio method, as shown on the right side of Fig. 6. At the processing temperatures from 500 to 600 °C, the sintering is unlikely to occur for WS_2 since WS_2 had a much high melting point of 1250 °C [23]. The interfacial bonding is weak at 500 and 520 °C, making the pull-out of some loose WS_2 from the Al matrix during sample preparation easy to occur. As a result, the percentages of WS_2 in SPS500 and SPS520 were less than 10 wt%, which will be further discussed later in the microstructural analysis section.

The microstructure of Al–WS_2 fabricated at various temperatures was observed by SEM, as shown in Fig. 7. The composite powder constituted Al powder satellited by WS_2, which was reflected in the microstructure of the bulk samples. WS_2 clusters were mainly located at the boundaries of the Al particles, outlining the individual particles and making their profiles discernible. Due to the lack of chemical bonds with Al, plenty of WS_2 clusters were lifted out from the SPS500 cross-section during metallographic preparation, leaving behind large voids, which accounts for the less WS_2 content on the surface determined by the XRD pattern (Fig. 6). With increasing the processing temperature to 520 °C, evidence for the pull-out of WS_2 was not detected, but boundary microvoids surrounded the WS_2 clusters. Further increase in the temperature to 540 °C and beyond showed the parts with no defects in the polished cross-sections, meaning a stronger interface between Al and WS_2. Furthermore, the volume of the reinforcement visible in the prepared cross-section was higher. This was particularly clear for SPS580 and SPS600 (Fig. 7e and f). This observation means that at higher temperatures, the interfacial reactions between Al and WS_2 through diffusion of the latter into the former. This is further supported by the findings reported in our earlier study [18].

The higher magnification images revealed the microstructure of the

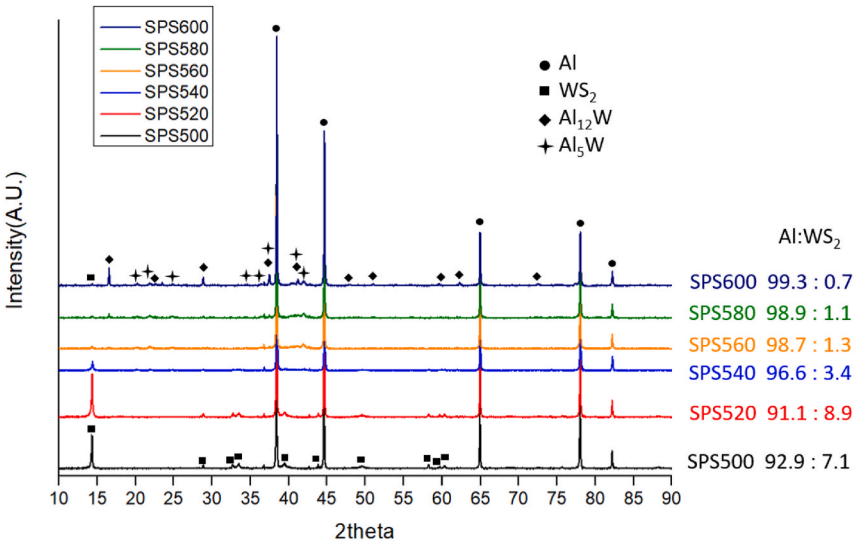

Fig. 6. XRD patterns and the phase weight ratio of Al and WS_2 in Al–WS_2 composites fabricated by SPS under 50 MPa at 500 °C, 520 °C, 540 °C, 560 °C, 580 °C, and 600 °C. With the increasing fabricating temperature, the intensities of the characteristic peaks for WS_2 were weakened, while the peaks of the intermetallic phase emerged at 540 °C and then their intensity strengthened. (Colour print required).

WS_2 clusters in the composite samples with the chemical analysis showing the elemental distribution in Fig. 8. Freestanding WS_2 were observed for SPS500 and SPS520 (Fig. 8a and b) as the EDX map showed regions where aluminium or, tungsten and sulphur were detected separately. When the fabricating temperature increased to 540 °C (Fig. 8c), an Al–W intermetallic shell structure between the reinforcement and matrix was observed with its distinguishable contrast compared to WS_2 and Al in the SEM image. This was also proven by the EDX map, where a shell between Al and WS_2 concurrently containing aluminium, tungsten, and sulphur can be identified. With further increase in the temperature from 560 °C to 580 °C, the thickness of these intermetallic shells increased, and the diffusion of WS_2 into Al was detectable, which led to the blurring of the boundary between the two constituents (Fig. 8d and e). When the temperature reached 600 °C, the amount of the intermetallic shell structure had the highest level but at the expense of most of the WS_2 content (Fig. 8f). The evolution of WS_2 in Al observed in these SEM images matrix is consistent with the findings from the XRD (Fig. 6) analysis.

The detailed microstructure of the intermetallic shell in sample SPS580, as a representative sample, was shown by TEM, as depicted in Fig. 9. In agreed with our previous work of investigating the interfacial structure of Al–WS_2 [18], the phases at this region existed with preferential crystal orientation around the WS_2 core (Fig. 9b), indicating they are *in-situ* formed via the reaction between Al and WS_2 at the interface. Higher magnification analysis of the shell forming at the interface between the Al matrix and the WS_2 reinforcement confirmed that the shell comprises two phases. The two different d-spacings for these distinctive phases were measured and determined to correspond to $Al_{12}W$ and Al_5W in Fig. 9d and f, respectively. This finding corresponds well with the XRD results in Fig. 6.

According to above observations, the microstructure evolution and interfacial reaction during the process are illustrated in Fig. 10. The volume shrinkage of the powder mixture firstly occurred in response to the pressure and elevated temperature, which resulted in some WS_2 clusters locating within the gaps among Al particles. As the temperature rose, these gaps closed due to improved densification before atomic level bonding started to take place, and the WS_2 on the grain boundary of Al particles started to diffuse through lattice, which is a typical process for sintering composite materials [24]. Finally, the WS_2 core-intermetallic shell-Al microstructure at the interface was formed with WS_2 diffusion length of 0 to approximately 5 μm depending on the process conditions (fabricating temperature 500–600 °C).

3.2. Hardness and tribological analysis of Al–WS_2 composites

3.2.1. Hardness

To investigate the hardness of the phases found in the fabricated composite, nano-indentation was performed on the Al matrix and WS_2 clusters of SPS500, and on the intermetallic structure in SPS600. The hardness of WS_2 has not been widely explored in the literature, although it is known that WS_2 itself is only a solid lubricant with soft nature [25]. WS_2 showed a lower hardness (0.39 ± 0.08 GPa) than Al (0.58 ± 0.03 GPa), but the *in-situ* formed Al–W composite shell had a significantly higher hardness of 2 ± 1 GPa. The presence of the Al–W metallic phases in the interphase shell explains its higher hardness. This is in agreement with studies in the literature that reported higher strength for the Al–W intermetallic phases compared to the Al matrix in Al–W composites [26]. Nevertheless, the nano-hardness of the intermetallic shell showed the most scatter in data. This could be attributed to the spatial variation composition of the intermetallic structure.

Enhancing the hardness of Al-based composite structures by introducing WS_2 as a reinforcement has been reported by several studies, such as [11]. A common explanation for the strengthening mechanism is that the WS_2 located along the grain boundaries of the Al matrix play a pinning role in restraining grain growth and impeding the dislocation motion [14], which enhances the material's strength, according to the Hall-Petch relationship. Nevertheless, it should be noted that recrystallization and grain growth were restrained during SPS [18], and the presence of the intermetallic structure is yet to be discussed. In this study, the micro-hardness showed a rising trend with increasing the fabrication temperature (Fig. 11). The highest micro-hardness was exhibited by the SPS600 (39 ± 1 HV), more than a 30 % increase in comparison with the SPS500 specimen (26 ± 1 HV). It is believed that the *in-situ* reaction, which produced a high-hardness intermetallic shell was the major contributor to the increase in the average hardness of the composites. According to the micro-hardness map, the hardness values on the tested cross-sections had a bimodal distribution with the majority of indents in the higher hardness range (Fig. 11a–c), but the scenario was rather the opposite at higher temperatures (Fig. 11d–f). This was attributed to the remarkable increase in hardness at the reinforcement-rich locations due to the increase of intermetallic shell and the decrease of soft WS_2 content at higher temperatures, which also

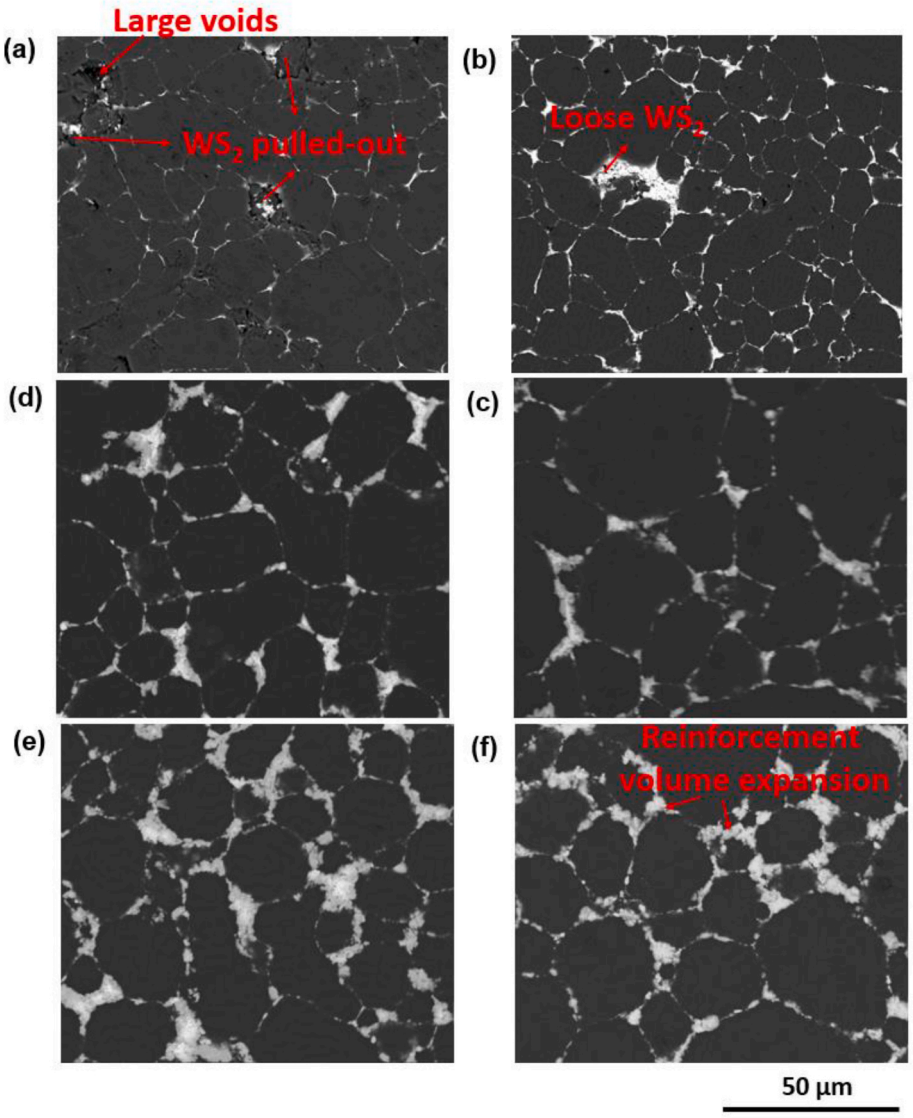

Fig. 7. Low magnification SEM images showing the microstructure of Al–WS_2 fabricated at various temperatures. (a) SPS500; (b) SPS520; (c) SPS540; (d) SPS560; (e) SPS580; (f) SPS600. These figures show the evolution of WS_2 in the Al matrix. The interaction between Al (dark regions) and WS_2 (white regions) enhances with increasing temperature, and the volume of the reinforcement expands due to the in-situ reaction between Al and WS_2 during SPS.

resulted in the monotone increase in the mean micro-hardness values with increased temperature. The nano- and micro-hardness results agreed, reinforcing the importance of the *in-situ* reaction occurring during SPS. This improved hardness is critical for the material's tribological behaviour.

3.2.2. *Tribological analysis*

The COF and specific wear rate of the SPS composites after 4000 cycles of sliding wear are summarised in Table 1. The decrease in the COF with increasing the fabrication temperature was marked from 500 to 580 °C, then it stabilised. Similarly but more remarkably, the wear rate demonstrated a 97 % decline when the fabrication temperature increased from 500 to 580 °C before there was a slight increase in wear rate when the temperature reached 600 °C, although it is traditionally believed that wear resistance should be proportional to the material's hardness. It is worthwhile to mention that the specific wear rates in this study are much higher than the desired range for intended applications (usually less than 10^{-9} $mm^3/N \cdot m$ is required [27]). This is expected as pure Al was used as the matrix material instead of Al alloys in this fundamental study, and these values are comparable to the previous reports for pure Al–WS_2 composites [11,15].

The development of wear behaviour in the Al–WS_2 parts was studied by wear track evolution analysis, as shown in Fig. 12 (enlarged images are displayed in Fig. S2). Notable differences were observed for the composites fabricated at various temperatures. SPS500 showed a low COF value of less than 0.5 at the beginning of sliding wear among all samples, but it gradually increased during sliding with a gradually increasing amplitude of fluctuation, while SPS560, SPS580, and SPS600 had a high COF value of more than 1.0 during the first 500–1000 cycles before the value significantly reduced to about 0.5 for the remaining course of sliding. This is because SPS500 contained the highest proportion of un-bonded WS_2, which was easily smeared onto the worn surface, leading to the low COF at the beginning. In contrast, due to the formation of the intermetallic structure with higher hardness, the abrasiveness between counterpart materials during sliding increased in a similar manner as hard ceramic reinforced Al MMCs [28]. Further on, the worn surface was relatively bright throughout the 4000 cycles of sliding wear for SPS500. Higher magnification images (marked as "*" in Fig. 12) show that the centre of the wear track was relatively bright, meaning the WS_2 was pushed to the ends of the track, piling up at the edges. This caused the increase in the contact area and thus ploughing effect on the worn surface between the counterpart materials, eventually

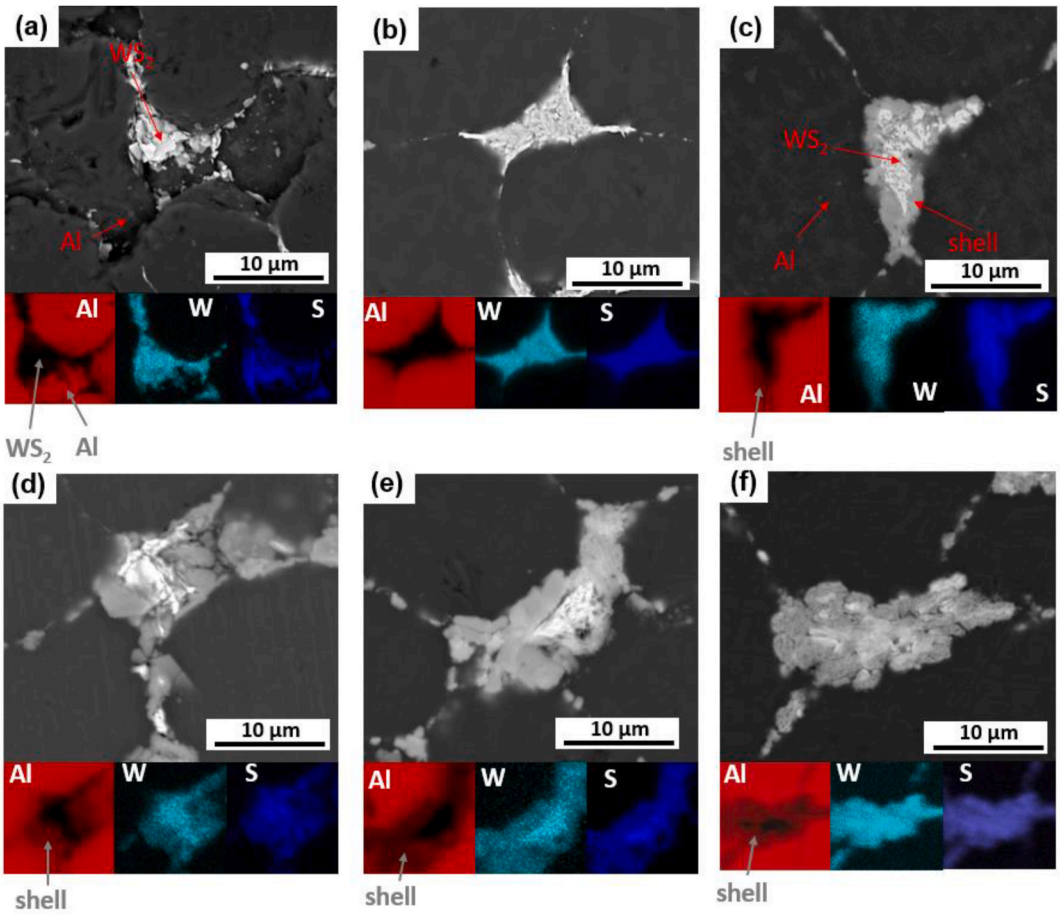

Fig. 8. High magnification SEM images showing the microstructure of reinforcement phases of Al–WS_2 fabricated at various temperatures. (a) SPS500; (b) SPS520; (c) SPS540; (d) SPS560; (e) SPS580; (f) SPS600. From 560 °C and above, the Al–W intermetallic phase started to form at the expense of WS_2. (Colour print required).

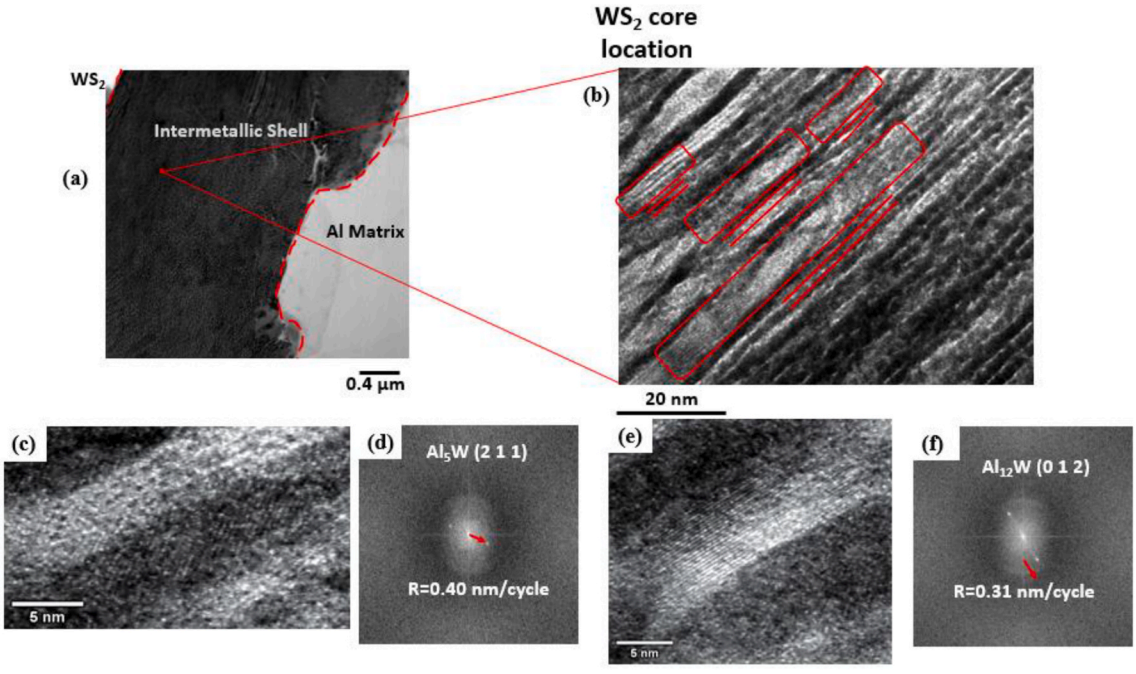

Fig. 9. TEM images showing the microstructure at the intermetallic shell. (a) lower magnification image showing the intermetallic shell-core region; (b) high magnification image revealing the crystal structures with preferred crystal orientations (indicated by "//"). (c) and (d) example of the crystal plane corresponding to Al_5W and its Fast Fourier transform (FFT) result; (e) and (f) example of the crystal plane corresponding to $Al_{12}W$ and its Fast Fourier transform (FFT) result. (Colour print required).

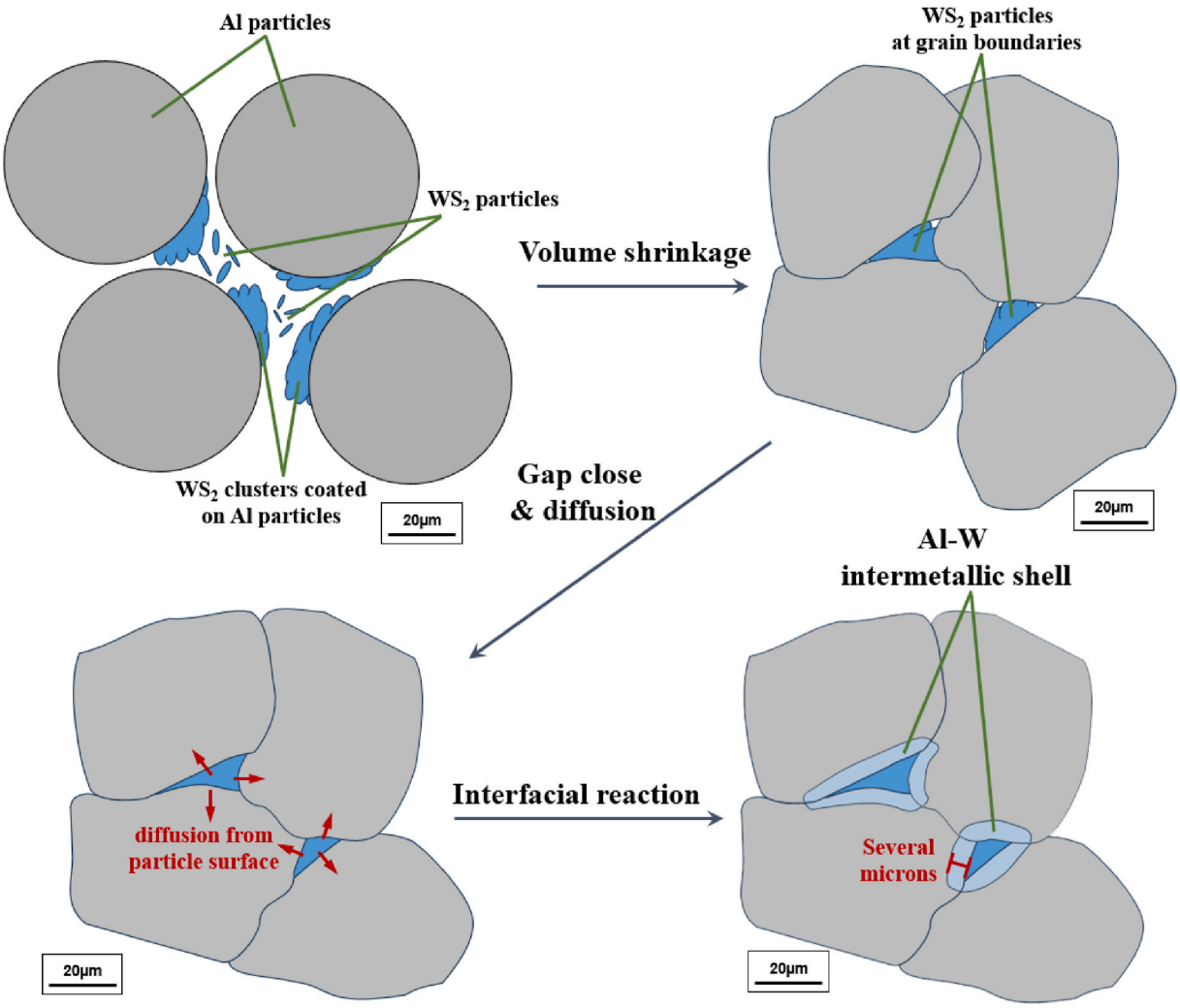

Fig. 10. Schematic showing the *in-situ* reaction occurred during SPS.

causing the constant rise of COF. On the other hand, a dark tribo-layer had formed on the surface of SPS560, SPS580, and SPS60 after the initial 500 cycles, which reduced the COF. The formation of this tribo-layer, also known as mechanically-mixed layer (MML) [29] is related to the reaction between the two countersurfaces and the oxidation of Al during friction, producing a darker region on the worn surface [11]. This layer is known to have high hardness and can greatly reduce friction and wear [30]. The tribo-layer broke down and later regenerated for SPS560 and SPS600, which can be observed from the wear track image (Fig. 12 dotted rectangular area) and caused the sudden rise in COF before it recovered to the previous steady value. However, no obvious sign of tribo-layer damage was detected for SPS580. This could be due to the inferior hardness of SPS560 that makes the tribo-layer vulnerable under loading, and the insufficient WS_2 in SPS600 that resulted in higher friction forces adverse to the tribo-layer. The combination of a desirable amount of hard intermetallic phases and solid lubricant makes the tribo-layer on SPS580 stable over the 4000 cycles sliding test. It is noteworthy that the lowest COF (0.55 ± 0.02) achieved in this work was also much lower than the comparable study in the literature where similar test condition was applied (COF = 0.66) [14]. This is potentially due to the added advantage in the current study from the presence of the intermetallic structure that may not have been realised in Vaziri et al. [14] since the processing temperature was set as low as 500 °C.

The evolution of wear behaviour was further validated by the *in-situ* wear volume analysis (Fig. 13). Interestingly, the wear volume for SPS500 increased almost linearly with the number of friction cycles, which follows the classic Archard's model [22] as described in Equation (4). However, the wear volume for SPS560, SPS580, and SPS600 was much lower, and the wear rates dropped over time, which does not follow Archard's model. This is due to the formation of the tribo-layers that increased the hardness of the worn surface [31]. Also, the data fluctuated when the tribo-layer breakdown occurred during the wear test for SPS560 and SPS600 (observed from the worn surface at corresponding cycles in Fig. 12) due to the asperities in contact that caused the variation in measurement. Afterwards, the wear rate reduced, resembling the previous manner as a result of the tribo-layer regeneration. This behaviour matches well with the observations in Fig. 12.

The morphology of the wear tracks on various samples at the end of the test can be seen in Fig. 14, with the EDX maps showing the distribution of W. For SPS500, significant amount of loose debris due to ploughing and plastic deformation was found to adhere to the rough worn surface. These feature, combined with the high wear rate of SPS500 (Table 1), indicates severe adhesive wear [32]. The amount of debris remarkably reduced for SPS560 and became difficult to trace for SPS580, and the main features on the surface gradually became shallow grooves, which suggests the transition from adhesive wear to mild abrasive wear with the enhanced hardness resulting from increasing the fabrication temperature. As previous study suggests, the mild abrasive wear shows steady COF during sliding and negligible wear loss [33]. This agrees with the COF curve (Fig. 12) and slow progression of wear volume (Fig. 13) observed for SPS580. However, micro-cracks were

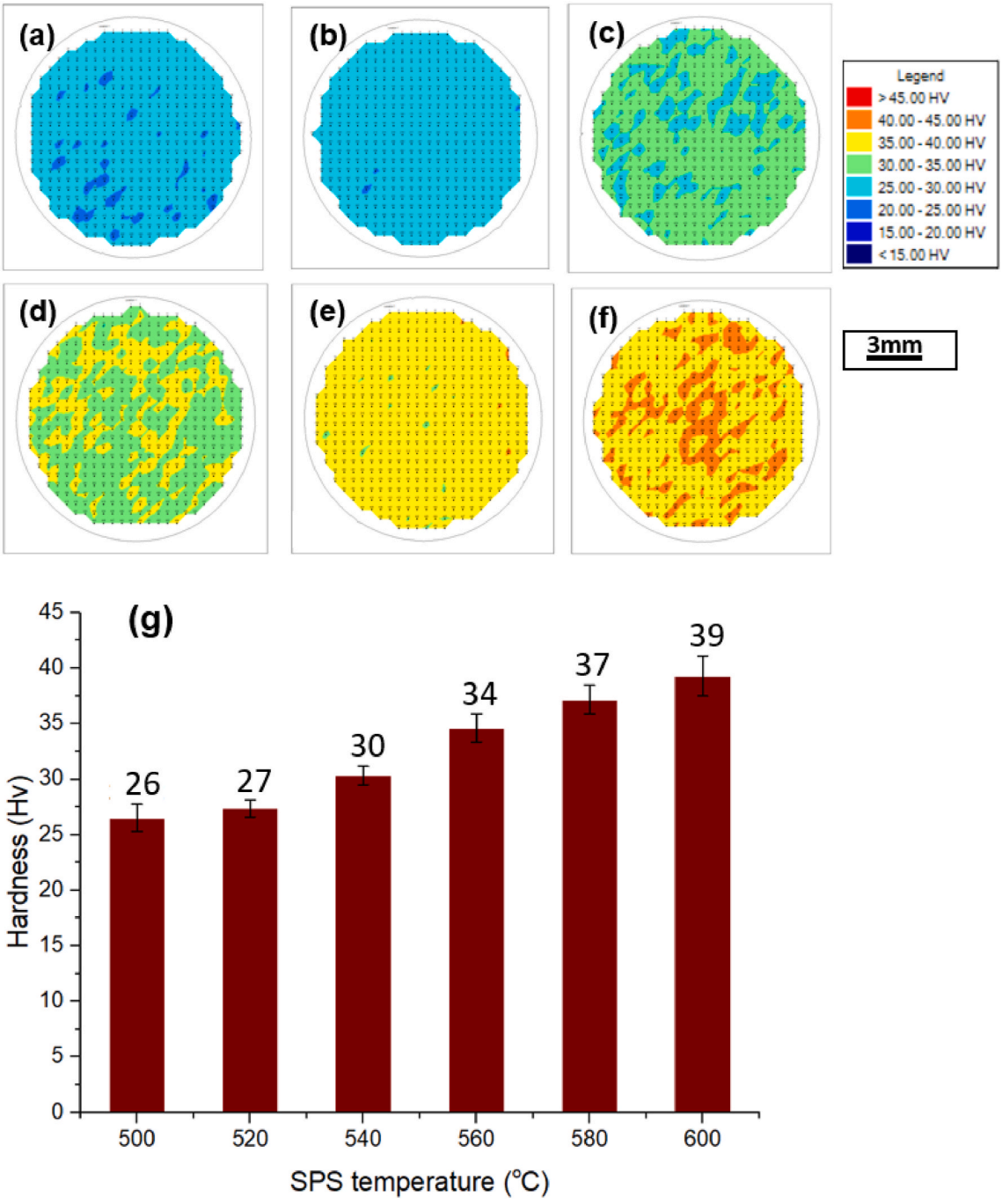

Fig. 11. Micro-harness maps of SPS Al–WS_2 samples fabricated at various processing temperatures. (a) SPS500; (b) SPS520; (c) SPS540; (d) SPS560; (e) SPS580; (f) SPS600; (g) Plot showing the variation of mean micro-hardness with the processing temperature. (Colour print required).

Table 1
Tribological test results of SPS samples fabricated using various conditions. Both COF and specific wear rates decreased with increasing the temperature until 580 °C.

Sample	Coefficient of friction	Specific wear rate × 10^{-3} $mm^3/N \cdot m$
SPS500	0.68 ± 0.01	75 ± 1
SPS520	0.66 ± 0.05	70 ± 2
SPS540	0.62 ± 0.02	24 ± 3
SPS560	0.59 ± 0.02	15 ± 1
SPS580	0.55 ± 0.02	2.1 ± 0.3
SPS600	0.56 ± 0.01	2.8 ± 0.6

easily observed on the surface for SPS600 since less lubricant remained in the microstructure as most of the WS_2 was consumed in the *in-situ* formation of the intermetallic phases ($Al_{12}W$ and Al_5W), which increased its tendency to delamination with higher friction forces. This worn surface morphology combined with the tribo-layer breakdown observed in Fig. 12 corroborates delamination wear [34] that occurred for SPS600. Moreover, the tribo-layer on the worn surface of different samples can be further revealed through elemental analysis. W was scattered in some specific locations over the SPS500 sample (white circles in Fig. 14a and b), having similar morphologies and sizes as the WS_2 clusters in the Al matrix before the wear test (Fig. 7a). And O, one the other hand, exited in the form of small particles. This suggests that WS_2 failed to spread and deposit on the surface and form a complete

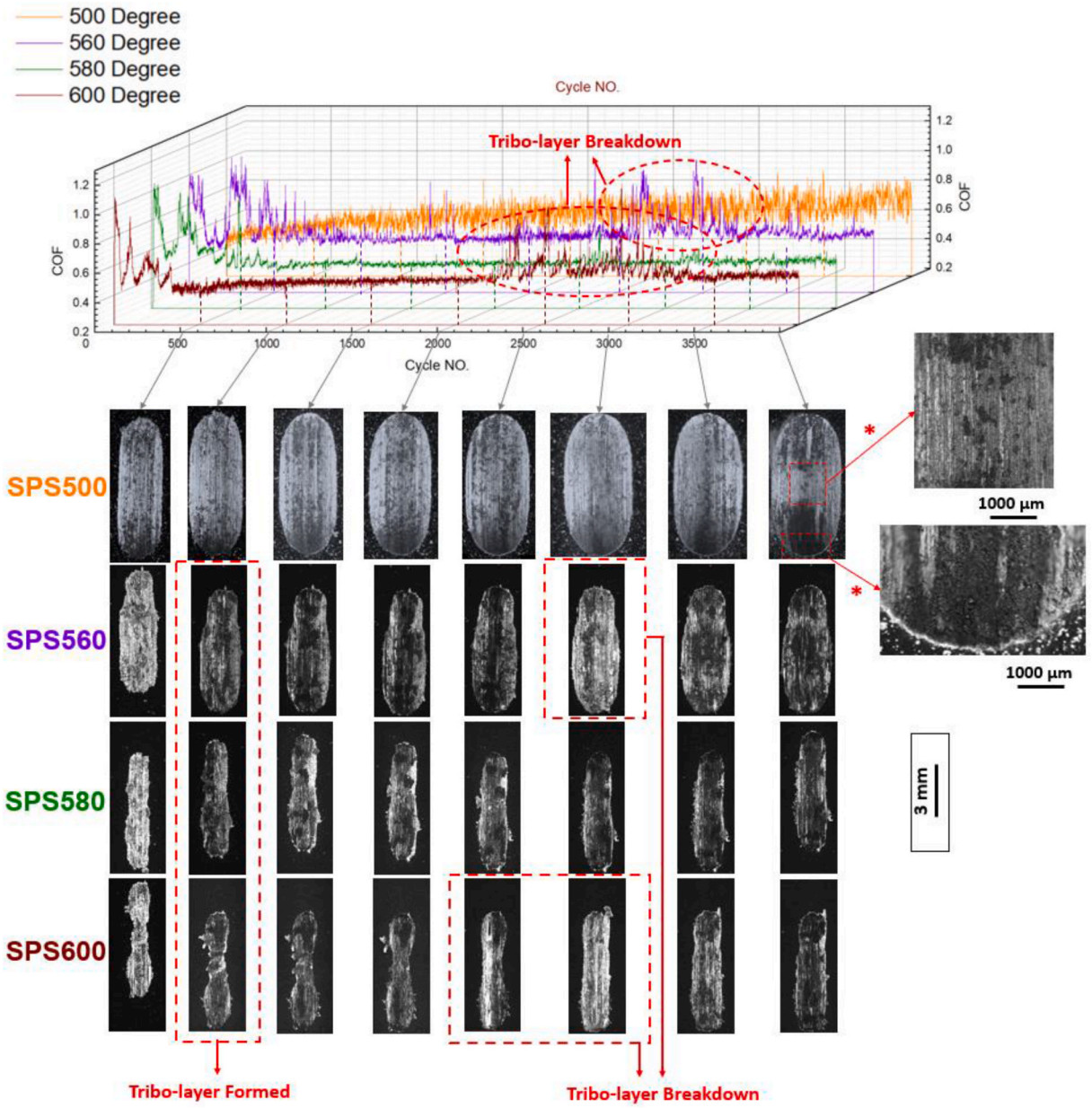

Fig. 12. In-situ wear track analysis on the Al–WS_2 samples fabricated at different temperatures. Tribo-layers were only formed for SPS560-600, and the tribo-layer breakdown was detected for SPS560 and SPS580. (Colour print required).

oxidised tribo-layer. However, for SPS560, SPS580 and SPS600, O and W was nearly evenly distributed over the worn surface (Fig. 14d, f, and h), which corroborate the findings in Fig. 12 that a uniform tribo-layer had been formed.

The depth profile of subsurfaces of various samples after wear tests is shown in the SEM images and EDX maps in Fig. 15. Except for SPS500 (Fig. 15a), all other samples, namely SPS560 (Fig. 15b), SPS580 (Fig. 15c), and SPS600 (Fig. 15d), had a wear-affected region enriched with reinforcement phases and oxides on the top, which was evident from the respective elemental distribution of W and O. This is attributed to the formation of Al–W intermetallic phases at the fabricating temperature of 560 °C and above that enhanced surface hardness (confirmed by XRD analysis, Fig. 6, and micro-hardness tests, Fig. 11). Therefore, unlike SPS500, these samples displayed better resistance to ploughing by the counterpart material, and the debris on the wear track were gathered locally on the top, forming a clear contrast to the materials below that had similar microstructures to the bulk material, as observed previously in Fig. 7. On the other hand, the generated tribo-layer can be traced by the distribution of O on the subsurface [35,36]. SPS500 showed a thin oxidised film of approximately 2 μm with weak intensity, indicating an unstable tribo-layer that barely accumulated during wear. With rising fabrication temperature, the amount of oxides on the top kept increasing until 580 °C when SPS580 exhibited the thickest tribo-layer of about 11 μm. This finding aligns well with the fact that SPS580 showed the most stable COF curve (Fig. 12) and lowest wear rate (Table 1), since a thick tribo-layer can significantly mitigate plastic deformation and thus friction and wear [11].

The difference among wear scars on the Si_3N_4 balls after sliding wear on various samples is displayed in Fig. 16. All scars are elliptical-shaped rather than circular since wear debris built up around the area where the wear track and surface of the ball in contact, thereby, debris subsequential re-adhered on the ball along the sliding direction during wear [37,38]. As expected, the width of wear scars notably decreased with rising processing temperatures of SPS parts from 500 °C to 580 °C, due to

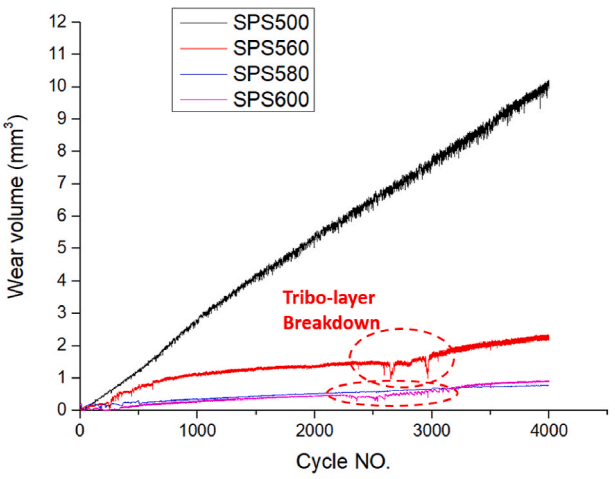

Fig. 13. In-situ wear volume on the Al–WS_2 samples fabricated at different temperatures. (Colour print required).

the surface hardness improvement of these composite materials (Fig. 11), which reduced their adhesion onto the counter-surface due to adhesive wear. Further elevating the processing temperature to 600 °C, however, did not witness a phenomenal difference in the wear scar size of the counter-surface, despite another increase in hardness for SPS600 compared to SPS580. This is attributed to the excessive interfacial reaction causing lack of WS_2, which contributed to more intensified friction between surfaces and gradually extended the contact region. Chemical analysis confirms the diminishing of Si and N elements on the scar due to the coverage of materials from composite worn surfaces. On the other hand, the accumulation of O on the scar is more remarkable for the balls sliding against SPS560, SPS580, and SPS600 (Fig. 16b, c, and e), compared to SPS500 (Fig. 16a). This suggests the effective formation of oxidised tribo-layer when Al–W intermetallic structure formed, which agrees with composite worn surface analysis (Fig. 14).

Based on the findings in this study, it can be assumed that the wear performance of the Al–WS_2 composites produced by SPS depends on two factors, the hardness and residual solid lubricant content after processing. The schematics showing the tribological behaviour of Al–WS_2 fabricated at various temperatures are illustrated in Fig. 17. At lower temperatures (500–520 °C, Fig. 17a), voids and defects in the low

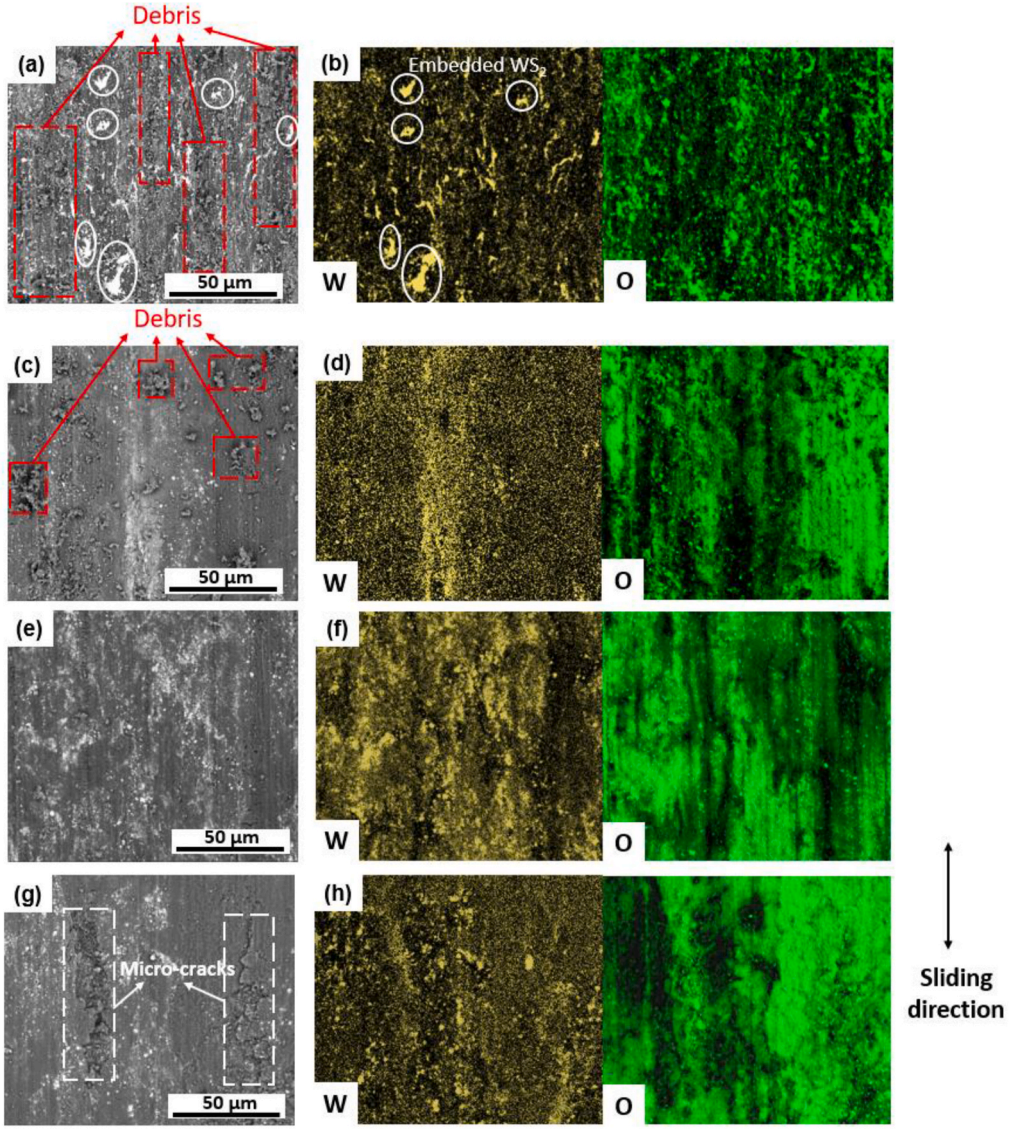

Fig. 14. SEM images of wear track morphology on various samples and the corresponding W and O elemental distribution map: (a) and (b) SPS500; (c) and (d) SPS 560; (e) and (f) SPS 580; (g) and (g) SPS600.

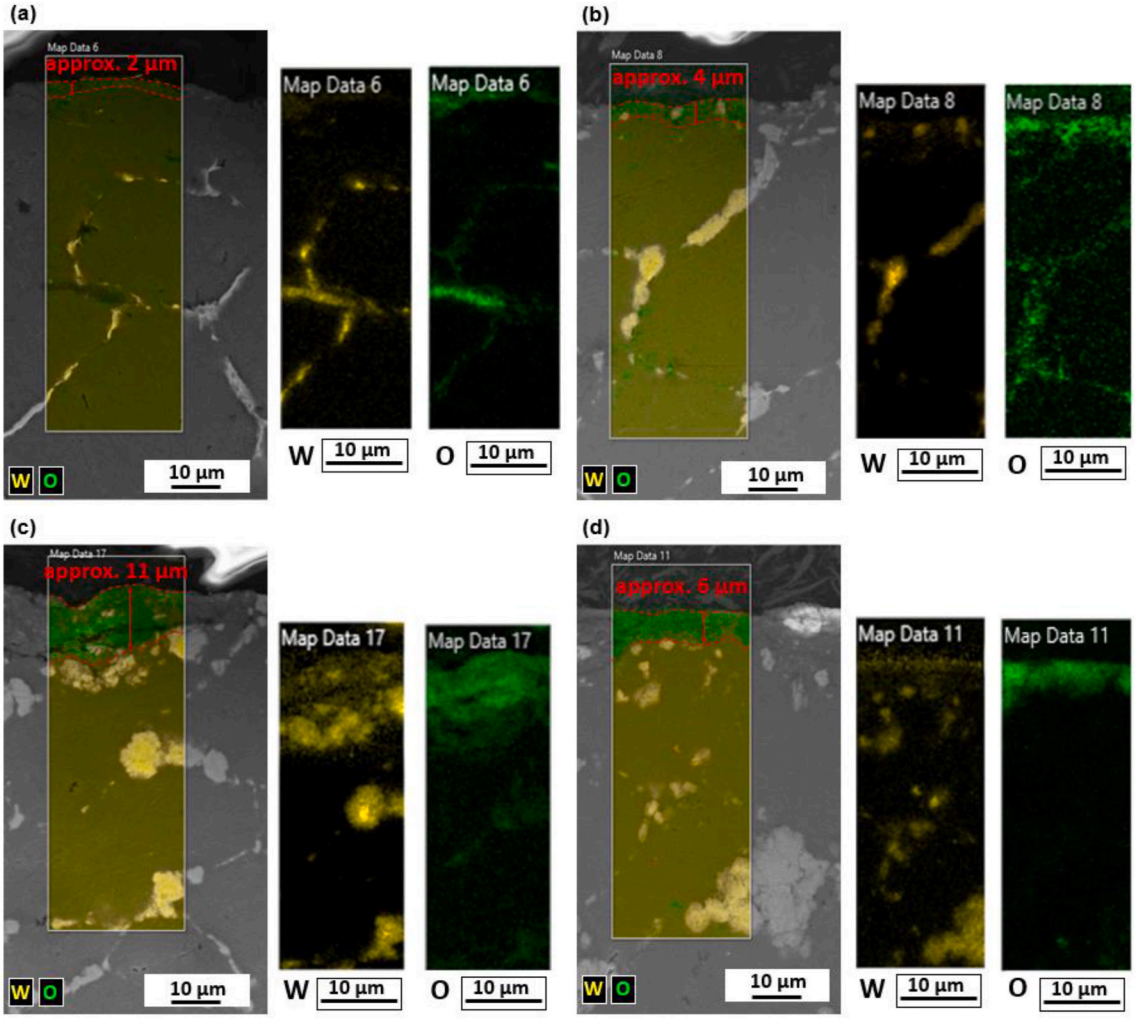

Fig. 15. SEM images of the cross-section vertical to the sliding direction and the corresponding W and O elemental distribution map: (a) SPS500; (b) SPS 560; (c) SPS 580; (d) SPS600. (Colour print required).

density parts increase the effective normal stress by reducing the actual contact area during sliding [39], which increases the wear rate. On the other hand, because the surface hardness is low, and the WS_2 particles lack a strong interfacial bonding with Al, the porosities acted as points of weakness that promote material removal from the surface, causing severe adhesive wear as analysed previously. The debris continue to be ploughed from the contact surface to the edges of the wear track by the counterpart material. Thereby, the worn surface is not sufficiently lubricated. For higher fabrication temperatures (560–580 °C, Fig. 17b), intermetallic shells/interphase form between the WS_2 particles and the Al matrix, which makes the surface more resistant to the load, thanks to the increase in hardness. Thereby, the wear debris is accumulated and smeared on the wear track, eventually generating a stable protective tribo-layer (Fig. 15c) and transforming the main wear mechanism from severe adhesive wear to mild abrasive wear. Also, the higher hardness constrains the plastic deformation introduced by friction, which reduced the adhesive forces between the specimen and the sliding ball, lowering the COF. However, an excessive increase in temperature (600 °C, Fig. 17c) leads to the majority of the solid lubricant being consumed in the formation of the intermetallic phases, diminishing the lubricating effect and leaving the tribo-layer more susceptible to cracking and breaking down by fatigue, leading to delamination on the worn surface as seen from the worn surface (Fig. 14g).

This study, therefore, highlights the critical role of the interrelationship between the process parameters during SPS production of composite materials (in this case, the temperature) and the resultant in-situ reactions when using self-lubricating additives to metal matrix composites. Although the formation of the intermetallic phases was favoured for increasing the composite material's hardness, this study showed how important it is to balance this transformation to retain an adequate amount of the self-lubricating additive to tailor the microstructure and realise a compromise for the overall tribological behaviour of the produced parts.

4. Conclusions

Engineering the tribological performance of SPS Al–WS_2 composites by tailoring the amount of *in-situ* reactions between the matrix and lubricants through controlling the processing temperature is presented for the first time. The key findings of this study are summarised as follows.

1. The microstructure of the composites can be controlled by varying the temperatures between 500 and 600 °C during processing. An intermetallic shell composed of Al_5W and $Al_{12}W$ formed at the interface between the Al matrix and the self-lubricating WS_2 particles, reducing the final content of WS_2 in the parts produced using 560 °C and above.
2. The intermetallic interphase in the microstructure exhibited a nanohardness higher than both Al and WS_2, which leads to a significant contribution to material's tribological performance since the wear

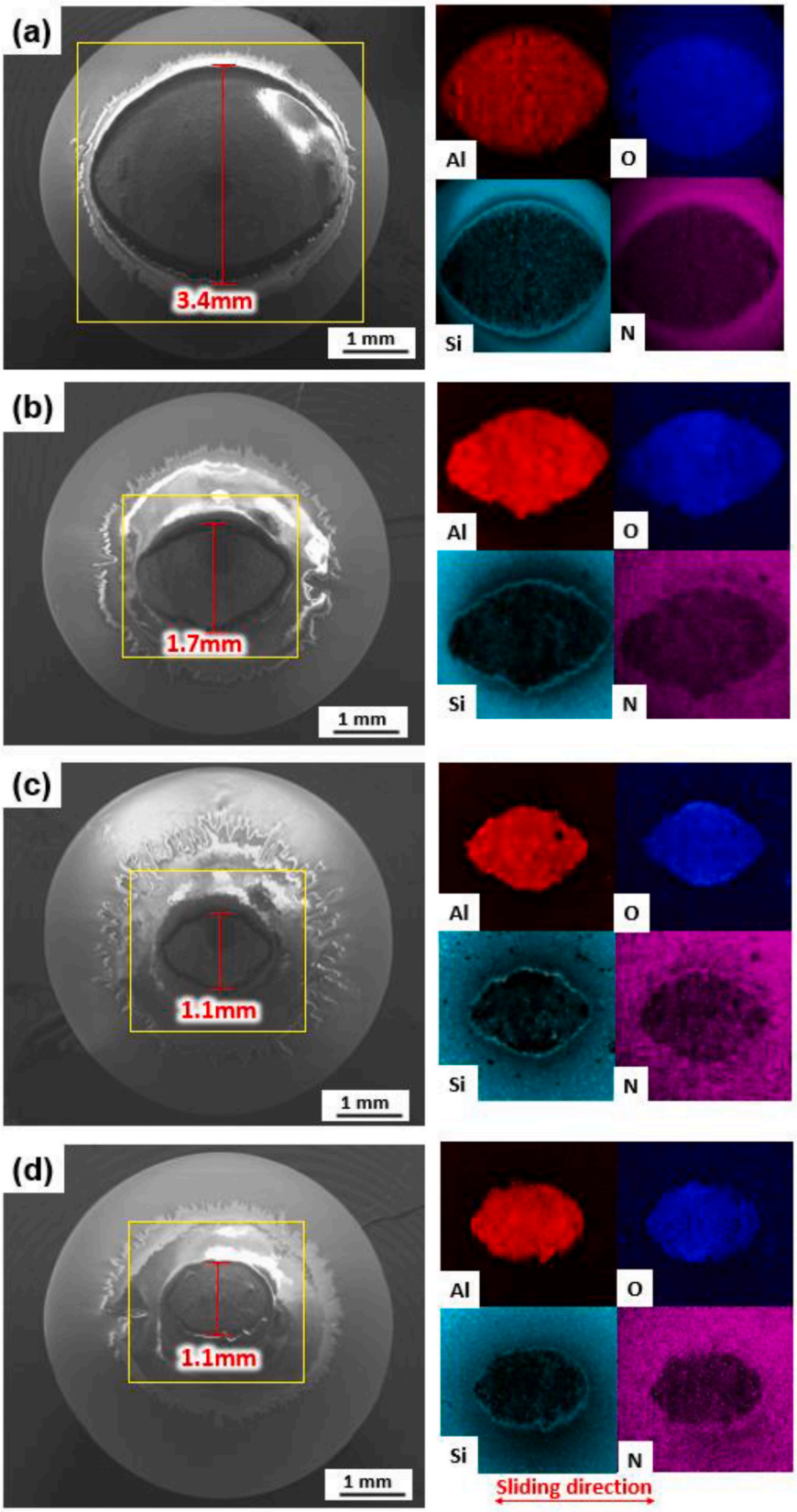

Fig. 16. SEM images of the $Si3N_4$ ball showing the scar after sliding wear on various samples and corresponding elemental distribution maps on the scar area. (a) SPS500, (b) SPS560, (c) SPS580, (d)SPS600. (Colour print required).

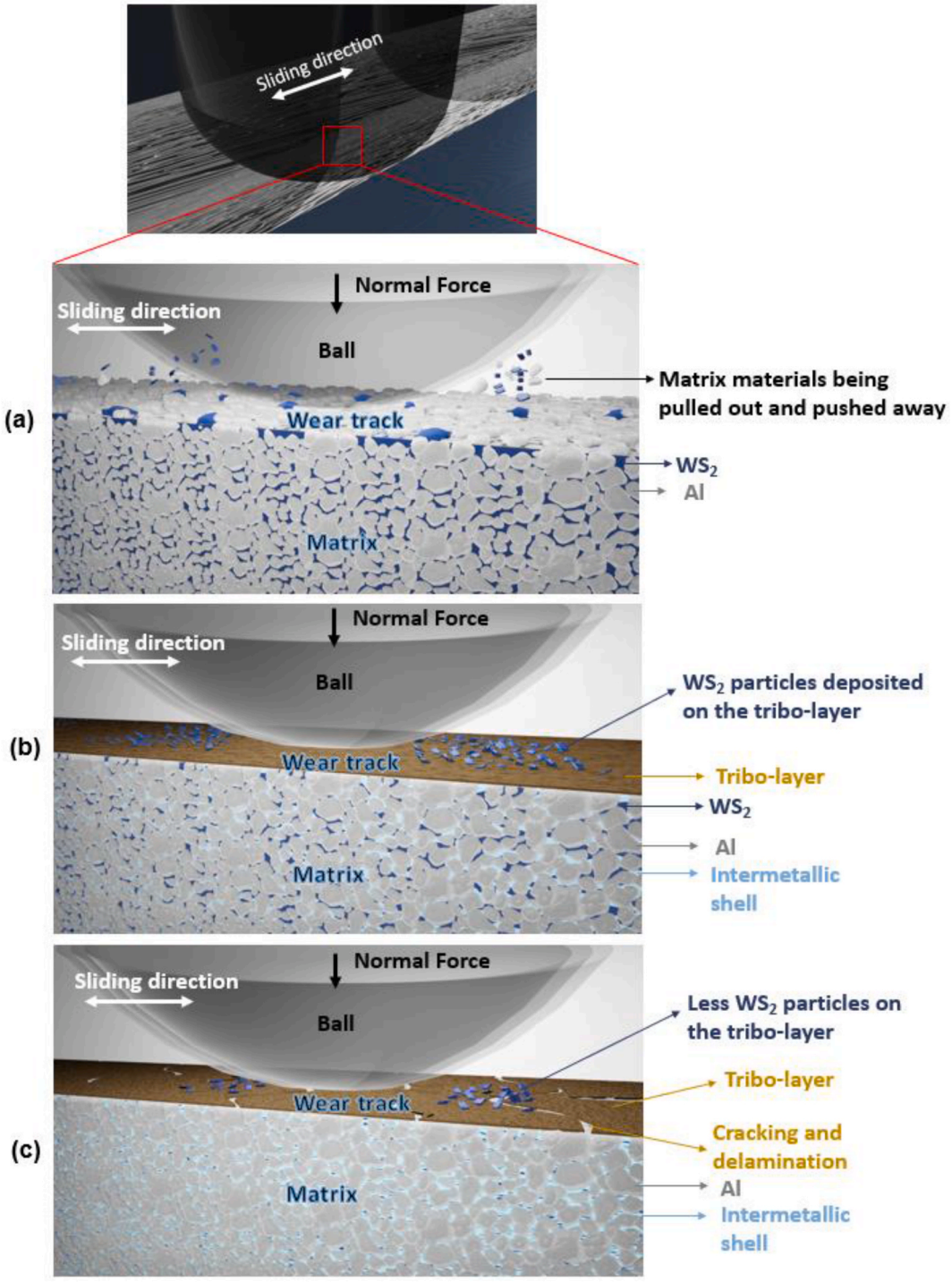

Fig. 17. Schematic illustrating the tribological behaviour of Al–WS_2 composites fabricated at various processing temperatures by SPS: (a) 500–520 °C; (b) 560–580 °C; (c) 600 °C. (Colour print required).

behaviour depended on both the overall hardness of the composite and the solid lubricant content. The best tribological performance was reached for Al–WS_2 parts fabricated at 580 °C, with a scar of minimum area on its counter-surface (Si_3N_4 ball), COF of 0.55 ± 0.02 and wear rate of (2.1 ± 0.3) × 10^{-3} mm^3/Nm.

3. From the wear track evolution analysis as well as microscopic observations of composite worn surfaces, it was confirmed that the Al–W intermetallic structure played a crucial role in the formation of tribo-layers during wear. An effective amount of intermetallic structure led to a uniform distribution of oxides on composite worn surfaces and noticeable accumulation of O on Si3N4 ball scars. The wear volume increased linearly with friction cycles at lower fabricating temperatures where the tribo-layer did not form, but it reduced progressively when the matrix was protected by the tribo-layer at higher fabrication temperatures.

This work provides a novel in-depth understanding of the interfacial reactions in an SPS composite material, which includes the microstructure tailoring of WS_2 reinforced MMCs. The interesting findings presented in this study will be beneficial for translation to domains in

which similar *in-situ* reactions during fabrication may occur, such as copper [40] and titanium [41] composites. Future studies will investigate the significance of the *in-situ* reactions in Al alloy composites since alloys are more prevalent for various applications and often exhibit higher strength than pure Al.

Declaration of competing interest

The authors declare that they have no known competing financial interests or personal relationships that could have appeared to influence the work reported in this paper.

Acknowledgements

This work was supported by Engineering and Physical Sciences Research Council (EPSRC) in Innovative Metal Processing, Centres of Doctoral Training (CDT) [Grant No: EP/L016206/1] for Peifeng Li; the University of Nottingham's Anne McLaren Fellowship for Nesma Aboulkhair. The authors of this work acknowledge the use of microscopy within the nano- and micro-scale research centre (nmRC) at the University of Nottingham. The authors also acknowledge the support provided by Loughborough Materials Characterisation Centre (LMCC) and for access to the Helios Plasma Focussed-Ion Beam (EPSRC grant EP/P030599/1). Thanks to Dr. Stuart Robertson from University of Loughborough for his help with Focused-Ion Beam milling and Transmission Electron Microscopy. All data created during this research are openly available from the University of Nottingham data repository at: DOI: 10.17639/nott.7349.

Appendix A. Supplementary data

Supplementary data to this article can be found online at https://doi.org/10.1016/j.jmrt.2023.10.157.

References

[1] Koli DK, Agnihotri G, Purohit R. Advanced aluminium matrix composites: the critical need of automotive and aerospace engineering fields. Mater Today Proc 2015;2(4–5):3032–41. https://doi.org/10.1016/j.matpr.2015.07.290.
[2] Taylor L, Dratva A, Spikes H. Friction and wear behavior of zinc dialkyldithiophosphate additive. Tribol Trans 2000;43(3):469–79. https://doi.org/10.1080/10402000008982366.
[3] Omrani E, Moghadam AD, Menezes PL, Rohatgi PK. Ecotribology. Springer; 2016. p. 63–103. https://doi.org/10.1007/978-3-319-24007-7_3.
[4] Tabandeh-Khorshid M, Omrani E, Menezes PL, Rohatgi PK. Tribological performance of self-lubricating aluminum matrix nanocomposites: role of graphene nanoplatelets. Eng Sci Tech Int J 2016;19(1):463–9. https://doi.org/10.1016/j.jestch.2015.09.005.
[5] Xiao J, Wu Y, Zhang W, Chen J, Zhang C. Friction of metal-matrix self-lubricating composites: relationships among lubricant content, lubricating film coverage, and friction coefficient. Friction 2020;8(3):517–30. https://doi.org/10.1007/s40544-019-0270-x.
[6] Prasad S, McConnell B. Tribology of aluminum metal-matrix composites: lubrication by graphite. Wear 1991;149(1–2):241–53. https://doi.org/10.1016/0043-1648(91)90377-7.
[7] Mahdavi S, Akhlaghi F. Effect of the graphite content on the tribological behavior of Al/Gr and Al/30SiC/Gr composites processed by in situ powder metallurgy (IPM) method. Tribol Lett 2011;44(1):1–12. https://doi.org/10.1007/s11249-011-9818-2.
[8] Liu E, Wang W, Gao Y, Jia J. Tribological properties of Ni-based self-lubricating composites with addition of silver and molybdenum disulfide. Tribol Int 2013;57:235–41. https://doi.org/10.1016/j.triboint.2012.08.014.
[9] Huang S, Feng Y, Liu H, Ding K, Qian G. Electrical sliding friction and wear properties of Cu–MoS2–graphite–WS2 nanotubes composites in air and vacuum conditions. Mater Sci Eng, A 2013;560:685–92. https://doi.org/10.1016/j.msea.2012.10.014.
[10] Zhao Z, Bai P, Misra RDK, Dong M, Guan R, Li Y, et al. AlSi10Mg alloy nanocomposites reinforced with aluminum-coated graphene: selective laser melting, interfacial microstructure and property analysis. J Alloys Compd 2019;792:203–14. https://doi.org/10.1016/j.jallcom.2019.04.007.
[11] Niste VB, Ratoi M, Tanaka H, Xu F, Zhu Y, Sugimura J. Self-lubricating Al-WS2 composites for efficient and greener tribological parts. Sci Rep 2017;7(1):1–14. https://doi.org/10.1038/s41598-017-15297-6.
[12] Wong K, Lu X, Cotter J, Eadie D, Wong P, Mitchell K. Surface and friction characterization of MoS2 and WS2 third body thin films under simulated wheel/rail rolling–sliding contact. Wear 2008;264(7–8):526–34. https://doi.org/10.1016/j.wear.2007.04.004.
[13] Mamedov V. Spark plasma sintering as advanced PM sintering method. Powder Metall 2002;45(4):322–8. https://doi.org/10.1179/003258902225007041.
[14] Vaziri HS, Shokuhfar A, Afghahi SSS. Investigation of mechanical and tribological properties of aluminum reinforced with Tungsten Disulfide (WS2) nanoparticles. Mater Res Express 2019;6(4):045018. https://doi.org/10.1088/2053-1591/aafa00.
[15] Rengifo S, Zhang C, Harimkar S, Boesl B, Agarwal A. Effect of WS2 addition on tribological behavior of aluminum at room and elevated temperatures. Tribol Lett 2017;65(3):76. https://doi.org/10.1007/s11249-017-0856-2.
[16] Domask AC, Cooley KA, Kabius B, Abraham M, Mohney SE. Room temperature van der Waals epitaxy of metal thin films on molybdenum disulfide. Cryst Growth Des 2018;18(6):3494–501. https://doi.org/10.1021/acs.cgd.8b00257.
[17] Prasad S, Asthana R. Aluminum metal-matrix composites for automotive applications: tribological considerations. Tribol Lett 2004;17(3):445–53. https://doi.org/10.1023/B:TRIL.0000044492.91991.f3.
[18] Li P, Xu F, Robertson S, Zhou Z, Hou X, Clare AT, et al. Metallurgical reactions and tribological properties of self-lubricating Al-WS2 composites: laser powder bed fusion Vs. spark plasma sintering. Mater Des 2022;110543. https://doi.org/10.1016/j.matdes.2022.110543.
[19] Samuels LE. Metallographic polishing by mechanical methods. 2003.
[20] ASTM International. Standard practice for instrumented indentation testing. West Conshohocken, Pennsylvania: Designation: E2546-07; 2007.
[21] ASTM International. ASTM G133-05. West Conshohocken, PA. 2016. ASTM G133-05.
[22] Archard J. Contact and rubbing of flat surfaces. J Appl Phys 1953;24(8):981–8. https://doi.org/10.1063/1.1721448.
[23] Eagleson M. Concise encyclopedia chemistry. Walter de Gruyter; 1994.
[24] Huo S, Wang Y, Yao M, Chen L, Kong Q, Ouyang J, et al. Reactive sintering behavior and enhanced densification of (Ti, Zr) B2–(Zr, Ti) C composites. J Eur Ceram Soc 2020;40(13):4373–80. https://doi.org/10.1016/j.jeurceramsoc.2020.05.037.
[25] Xiao J-K, Zhang W, Zhang C. Microstructure evolution and tribological performance of Cu-WS2 self-lubricating composites. Wear 2018;412:109–19. https://doi.org/10.1016/j.wear.2018.07.024.
[26] Zhang H, Feng P, Akhtar F. Aluminium matrix tungsten aluminide and tungsten reinforced composites by solid-state diffusion mechanism. Sci Rep 2017;7(1):1–8. https://doi.org/10.1038/s41598-017-12302-w.
[27] Kauzlarich J, Williams J. Archard wear and component geometry. Proc IME J J Eng Tribol 2001;215(4):387–403. https://doi.org/10.1243/1350650011543628.
[28] Ravindran P, Manisekar K, Rathika P, Narayanasamy P. Tribological properties of powder metallurgy–Processed aluminium self lubricating hybrid composites with SiC additions. Mater Des 2013;45:561–70. https://doi.org/10.1016/j.matdes.2012.09.015.
[29] Deuis R, Subramanian C, Yellup J. Dry sliding wear of aluminium composites—a review. Compos Sci Technol 1997;57(4):415–35. https://doi.org/10.1016/S0266-3538(96)00167-4.
[30] Ghazali M, Rainforth W, Omar M. A comparative study of mechanically mixed layers (MMLs) characteristics of commercial aluminium alloys sliding against alumina and steel sliders. J Mater Process Technol 2008;201(1–3):662–8. https://doi.org/10.1016/j.jmatprotec.2007.11.158.
[31] Liu Y, Liskiewicz TW, Beake BD. Dynamic changes of mechanical properties induced by friction in the Archard wear model. Wear 2019;428–429:366–75. https://doi.org/10.1016/j.wear.2019.04.004.
[32] Dwivedi D. Adhesive wear behaviour of cast aluminium–silicon alloys: overview. Mater Des 2010;31(5):2517–31. https://doi.org/10.1016/j.matdes.2009.11.038. 1980-2015.
[33] Kayaba T, Hokkirigawa K, Kato K. Analysis of the abrasive wear mechanism by successive observations of wear processes in a scanning electron microscope. Wear 1986;110(3–4):419–30. https://doi.org/10.1016/0043-1648(86)90115-8.
[34] Fleming J, Suh N. Mechanics of crack propagation in delamination wear. Wear 1977;44(1):39–56. https://doi.org/10.1016/0043-1648(77)90083-7.
[35] Bai P, Jin Y, Zhao Z, Li L, Liang M, Liao H, et al. Microstructure and tribological behavior of graphene/Al composites produced by selective laser melting. Mater Res Express 2019;6(10):1065c1061. https://doi.org/10.1088/2053-1591/ab3ef5.
[36] Wu L, Zhao Z, Bai P, Zhao W, Li Y, Liang M, et al. Wear resistance of graphene nano-platelets (GNPs) reinforced AlSi10Mg matrix composite prepared by SLM. Appl Surf Sci 2020;503:144156. https://doi.org/10.1016/j.apsusc.2019.144156.
[37] Mahade S, Awe SA, Björklund S, Lukáč F, Mušálek R, Joshi S. Sliding wear behavior of a sustainable Fe-based coating and its damage mechanisms. Wear 2022;500–501:204375. https://doi.org/10.1016/j.wear.2022.204375.
[38] Mahade S, Mulone A, Björklund S, Klement U, Joshi S. Novel suspension route to incorporate graphene nano-platelets in HVAF-sprayed Cr3C2–NiCr coatings for superior wear performance. J Mater Res Technol 2021;13:498–512. https://doi.org/10.1016/j.jmrt.2021.04.096.

[39] Deshpande PK, Lin RY. Wear resistance of WC particle reinforced copper matrix composites and the effect of porosity. Mater Sci Eng, A 2006;418(1):137–45. https://doi.org/10.1016/j.msea.2005.11.036.
[40] Wang Q, Chen M, Shan Z, Sui C, Zhang L, Zhu S, et al. Comparative study of mechanical and wear behavior of Cu/WS2 composites fabricated by spark plasma sintering and hot pressing. J Mater Sci Technol 2017;33(11):1416–23. https://doi.org/10.1016/j.jmst.2017.06.014.
[41] Gao Q, Yan H, Qin Y, Zhang P, Guo J, Chen Z, et al. Laser cladding Ti-Ni/TiN/TiW + TiS/WS2 self-lubricating wear resistant composite coating on Ti-6Al-4V alloy. Opt Laser Technol 2019;113:182–91. https://doi.org/10.1016/j.optlastec.2018.12.046.